PERGAMON

International Journal of Solids and Structures 39 (2002) 5719–5736

INTERNATIONAL JOURNAL OF SOLIDS and STRUCTURES

www.elsevier.com/locate/ijsolstr

An efficient numerical model for contact-induced crack propagation analysis

L.A. de Lacerda [a], L.C. Wrobel [b,*]

[a] *Instituto de Tecnologia para o Desenvolvimento, LACTEC/AMAT, Centro Politécnico da UFPR, Cx.P. 19067, Curitiba, PR, Brazil*
[b] *Department of Mechanical Engineering, Brunel University, Uxbridge, Middlesex UB8 3PH, UK*

Received 23 January 2002; received in revised form 8 July 2002

Abstract

This paper presents an efficient boundary element formulation for the simulation of contact-induced crack propagation problems. The formulation combines a load-scaling boundary element technique for frictional contact analysis and a dual boundary element method for axisymmetric crack propagation. These previously developed contact and fracture mechanics algorithms are revisited and adapted for the proposed coupled formulation. The novelty of the present work is the development of an efficient algorithm capable of simulating contact-induced crack propagation, while keeping proper equilibrium conditions in the frictional contact area. An efficient combination of the two separate formulations is not straightforward, and possible approaches are explained. The algorithm is validated by comparing the results of several indentation tests with available experimental data and analytical expressions. Its efficiency is also verified in frictional, conforming and non-conforming, indentation simulations.

Keywords: Boundary element method; Indentation tests; Axisymmetry; Contact; Crack propagation; Friction

1. Introduction

Indentation tests are commonly used as a technique for the assessment of material fracture properties. Different types of indenters exist, and the shapes of the microcracks initiated by them are inherent to their geometry. In particular, the indentation of brittle solids by relatively hard spherical and flat-tipped indenters may induce the growth of cone cracks. The controlled application of the indenter load is correlated to the cone crack base radii, during slow propagation, through the solid material fracture toughness (Lawn, 1993).

Several boundary element formulations for contact mechanics have appeared since the early eighties (Andersson, 1981; Abdul-Mihsein et al., 1986; Wrobel and Aliabadi, 2002). de Lacerda and Wrobel (2000) developed an efficient approach for axisymmetric problems, applicable to linear elastic materials, in which an incremental load-scaling technique is used to guarantee the proper traction behaviour at the edge of the frictional contact area.

* Corresponding author. Tel.: +44-1895-274000; fax: +44-1895-256392.
E-mail address: luiz.wrobel@brunel.ac.uk (L.C. Wrobel).

0020-7683/02/$ - see front matter
PII: S0020-7683(02)00465-1

A dual boundary element formulation for axisymmetric fracture mechanics has been recently presented by de Lacerda and Wrobel (2002). This particular technique is well suited for the computation of stress intensity factors with great accuracy, and for the analysis of crack propagation problems with great efficiency. The accuracy and efficiency of the dual method are higher than that of boundary element algorithms based on domain subdivision, since fictitious discretizations are not introduced and re-meshing is as simple as adding a couple of elements to the model, causing lesser modifications to the original system of equations (Portela et al., 1991).

Recently, Bush (1999) analysed frictionless contact-induced crack propagation problems with a BEM domain subdivision technique. In the present work, the coupling of the aforementioned frictional contact and dual BEM fracture mechanics formulations is performed, with the objective of modelling indentation tests. An algorithm for this coupling is proposed, and the dual formulation is adapted to account for the resulting incremental procedure. The keypoint in this development is to aggregate the efficiency of both formulations into the proposed algorithm. In this sense, the frictional effects in the contact area introduce some difficulties, as well as requirements concerning the type of crack elements which must be added during propagation. These matters are discussed in detail in later sections, through applications to different indentation tests.

2. Contact model

Consider an elastic body Ω subject to constraints and external loads along its boundary Γ. In the absence of volume forces, the displacement boundary integral equation describing the problem is of the form

$$C_{ij}(\boldsymbol{\xi})u_j(\boldsymbol{\xi}) = \int_\Gamma \lambda U_{ij}(\boldsymbol{\xi},\mathbf{x})t_j(\mathbf{x})\,\mathrm{d}\Gamma - \barint_\Gamma \lambda T_{ij}(\boldsymbol{\xi},\mathbf{x})u_j(\mathbf{x})\,\mathrm{d}\Gamma \tag{1}$$

where $U_{ij}(\boldsymbol{\xi},\mathbf{x})$ and $T_{ij}(\boldsymbol{\xi},\mathbf{x})$ are the displacement and traction fundamental solutions at a field point $\mathbf{x}$ due to a unit load applied at a boundary point $\boldsymbol{\xi}$, the free term $C_{ij}(\boldsymbol{\xi})$ is dependent on the geometry at $\boldsymbol{\xi}$, $u_j(\mathbf{x})$ and $t_j(\mathbf{x})$ are the displacements and tractions over the boundary Γ, and the sign on the second integral indicates Cauchy principal value. In two-dimensional analyses $i,j = x,y$ and $\lambda = 1$, while in axisymmetric analyses $i,j = r,z$ and $\lambda = 2\pi r_{\mathbf{x}}$, with r and z being the radial and axial coordinates, respectively, and $r_{\mathbf{x}}$ being the radial distance from the field point $\mathbf{x}$ to the axis of symmetry z. Depending on the type of analysis, different expressions are applicable to the tensors $U_{ij}(\boldsymbol{\xi},\mathbf{x})$, $T_{ij}(\boldsymbol{\xi},\mathbf{x})$ and $C_{ij}(\boldsymbol{\xi})$. For axisymmetric problems, U_{ij} and T_{ij} are given in terms of complete elliptic integrals, and the singularity behaviour of these tensors depends on the position of $\boldsymbol{\xi}$. If the collocation point $\boldsymbol{\xi}$ is not at the axis of symmetry, their singularity behaviour is similar to their two-dimensional counterparts. When $\boldsymbol{\xi}$ is on the z-axis the radial components U_{ri} and T_{ri} vanish, whereas the axial components U_{zi} and T_{zi} correspond to the three-dimensional fundamental solutions. However, the presence of λ in the integrand makes the integration of λU_{zi} bounded, while the integration of λT_{zi} is apparently comparable to two-dimensional ones. The latter can actually be proven to be bounded, since the radial displacement at this point is zero.

Now, consider a system of two or more elastic bodies in contact, in equilibrium under external loads and constraints. Problems involving contact can be categorized in different ways depending on characteristics such as the geometry of the contacting surfaces, the presence of friction and loading history. Generally, algorithms for the solution of contact problems should include a stepwise application of external loads, although there are particular cases, regarding the previous characteristics, in which a single step may be sufficient.

In the present work, special attention is given to non-conforming frictional contacts where the final extent of the contact area is not known a priori, and depends on the magnitude of the applied external forces. Furthermore, the presence of friction implies the development of shear stresses whose magnitudes

may lead to relative tangential displacements at the contact interface, and which are also dependent on the load history. This load dependence of the analysis makes it non-linear, requiring the subdivision of the external loads for its solution,

$$P^m = \sum_{k=1}^{m} \Delta P^k = P^{m-1} + \Delta P^m \tag{2}$$

where P^m represents all external loads at the final stage. As a consequence of this load discretization, displacements and tractions are also subdivided:

$$\begin{aligned} u_j^m(\mathbf{x}) &= u_j^{m-1}(\mathbf{x}) + \Delta u_j^m(\mathbf{x}) \\ t_j^m(\mathbf{x}) &= t_j^{m-1}(\mathbf{x}) + \Delta t_j^m(\mathbf{x}) \end{aligned} \tag{3}$$

where it is clear that each load increment ΔP^k results in changes to the displacements and tractions fields corresponding to Δu_j^k and Δt_j^k, respectively. From this subdivision, it is straightforward to derive an incremental boundary integral equation in the form

$$C_{ij}(\boldsymbol{\xi})\Delta u_j^k(\boldsymbol{\xi}) = \int_\Gamma \lambda U_{ij}(\boldsymbol{\xi}, \mathbf{x})\Delta t_j^k(\mathbf{x})\,\mathrm{d}\Gamma - \oint_\Gamma \lambda T_{ij}(\boldsymbol{\xi}, \mathbf{x})\Delta u_j^k(\mathbf{x})\,\mathrm{d}\Gamma \tag{4}$$

Subdividing Γ into a series of boundary elements and choosing appropriate functions to represent the displacements and tractions within each element, Eq. (4) can be used to build a system of equations which, together with boundary and contact conditions, is solved to obtain the unknown variables all over the boundaries. Contact conditions are composed of equilibrium and compatibility equations. Equilibrium equations are invariant and must be satisfied throughout the contact region at every step of the analysis. At any step k, they read

$$\Delta t_j^k(\mathbf{a}) - \Delta t_j^k(\mathbf{b}) = -\left(t_j^{k-1}(\mathbf{a}) - t_j^{k-1}(\mathbf{b})\right) \tag{5}$$

where **a** and **b** are the contacting points between two bodies. Compatibility conditions at any pair **ab** change according to the contact status at this position, which may also change during the load incrementation process. These conditions are

$$\Delta t_j^k(\mathbf{a}) = -t_j^{k-1}(\mathbf{a}) \tag{6}$$

for the *separate* status,

$$\begin{aligned} \Delta t_t^k(\mathbf{a}) \pm \mu \Delta t_n^k(\mathbf{a}) &= -\left(t_t^{k-1}(\mathbf{a}) \pm \mu t_n^{k-1}(\mathbf{a})\right) \\ \Delta u_n^k(\mathbf{a}) + \Delta u_n^k(\mathbf{b}) &= -\left(u_n^{k-1}(\mathbf{a}) + u_n^{k-1}(\mathbf{b})\right) \end{aligned} \tag{7}$$

for the *slip* status, where the subscripts t and n indicate the tangential and normal local directions and μ is the friction coefficient, and

$$\Delta u_j^k(\mathbf{a}) + \Delta u_j^k(\mathbf{b}) = -\left(u_j^{k-1}(\mathbf{a}) + u_j^{k-1}(\mathbf{b})\right) \tag{8}$$

for the *stick* status.

Assuming m is the number of load steps, m sets of results for $\Delta u_j^m(\mathbf{x})$ and $\Delta t_j^m(\mathbf{x})$ need to be calculated. At each step k the contact conditions, depicted in Eqs. (5)–(8), will depend on the total contact profile at the previous step $k-1$.

Single step analyses ($m = 1$) fail to provide (when $\mu \neq 0$) accurate tangential displacements and stresses, and further restrictions to its applicability will be seen when crack propagation is added to the problem. Multiple steps ($m > 1$) are essential for an accurate analysis. Different criteria can be used to define the load increments ΔP^k. Here, node to node contact elements and a load-scaling technique are used to calculate these increments. The basic idea of this technique is to use a linear extrapolation function to obtain a normal traction value very close to zero at the pair of nodes at the edge of the contact area.

Consider two neighbouring contact node pairs, where one of the node pairs is joined at the edge of the current contact area, and the other pair is the next to be joined once the load is incremented. The applied load at this stage is αP^m $(0 < \alpha < 1)$, and the necessary increment ΔP^k for this task is required. The second pair of nodes is set to slip contact conditions, to mark the new edge of the contact area. Initially, an arbitrary load βP^m $(\beta > \alpha)$ is applied and a normal traction value $t_n^{(1)}$ at the second node pair is obtained. Afterwards, another arbitrary value γP^m $(\gamma > \beta)$ is applied to produce $t_n^{(2)}$. Using these values and an extrapolation formula the required load increment to close the node gap, achieving t_n very close to zero, can be calculated from $\Delta P^k = (\delta - \alpha)P^m$ as follows:

$$\delta = \beta + (\gamma - \beta)\frac{t_n^{(1)}}{t_n^{(1)} - t_n^{(2)}} \tag{9}$$

A single application of this procedure is usually sufficient to get $t_n \cong 0$, unless the discretization is not refined enough. An advantage of this extrapolation over other incrementation techniques is that it avoids overloading or underloading at each load step. A disadvantage is that the final extrapolated load will probably be different from the designed one, but this can be corrected with a relocation of the final contact node pair. Another particularity is that, for every different load value ($\beta P, \gamma P$ or δP), only the independent vector of the system of equations is changed. Therefore, using an appropriate solver, once the system decomposition is performed, only the backsubstitution phase needs to be repeated to solve the system for each trial load.

The number of incremental load steps is directly proportional to the number of contact node pairs to be joined. The higher the number of contact node pairs, the smaller the load increments, the better the accuracy and the longer the computational time.

At each load step, an iterative procedure is still necessary to find the correct partitioning of stick and slip regions. Given a load step, the slip region is composed by contact node pairs that have experienced a relative tangential displacement, while at the stick region node pairs have not experienced the same sort of relative displacement. In this iteration process, compatibility contact equations are changed appropriately. Slip mode is assumed if the following test is not verified at stick mode pairs,

$$|t_t^k(\mathbf{a})| \leqslant |\mu t_n^k(\mathbf{a})| \tag{10}$$

On the other hand, stick mode is assumed if contact pairs in slip mode do not satisfy the relation:

$$t_t^k(\mathbf{a})(\Delta u_t^k(\mathbf{a}) + \Delta u_t^k(\mathbf{b})) \leqslant 0 \tag{11}$$

From Eq. (4), it can be seen that the integrations do not change during the incremental process, only the compatibility contact equations may be modified. An LU solver is quite attractive for this scheme where trial loads are employed (provided the size of the problem is not a restriction to the application of $O(N^3)$ solvers). However, to perform a new LU decomposition every time a compatibility equation is modified is a very expensive task. Fortunately, these modifications are usually very small compared to the number of equations in the system, and this feature gives room to the application of special algorithms to speed-up the analysis (Ezawa and Okamoto, 1989). de Lacerda and Wrobel (2000) described an algorithm which complies with the incremental history, and the suitability of such scheme to crack propagation analysis will be investigated later.

3. Crack model

Different boundary element techniques can be used to model fracture mechanics problems. The dual BEM is a very attractive method since discretizations are entirely restricted to the boundaries, which makes the computations more accurate. Another advantage is the easy 're-meshing' on crack propagation analysis, not only because of the reduced dimensionality of the problem, but also because the current mesh can be

preserved when crack increments are added. The dual BEM basically consists on the simultaneous application of the displacement and traction boundary integral equations to the crack boundaries (Portela et al., 1991), giving rise to a mathematically well-posed formulation.

Traction equations have been derived for two-dimensional and axisymmetric elasticity (Portela et al., 1991; de Lacerda and Wrobel, 2001). In both cases, continuity requirements for the displacement derivatives must be satisfied, and this is guaranteed by enforcing boundary smoothness at the collocation nodes. Therefore, discontinuous elements (edge collocation nodes shifted towards the centre of the element) are employed to model the cracks, wherever necessary.

In the absence of body forces, the traction boundary integral equation reads,

$$\frac{1}{2}t_i(\boldsymbol{\xi}) = m_k \oint_{\Gamma} \lambda D_{ikj}(\boldsymbol{\xi},\mathbf{x}) t_j(\mathbf{x})\,\mathrm{d}\Gamma - m_k \neq\!\!\!\!\int_{\Gamma} \lambda S_{ikj}(\boldsymbol{\xi},\mathbf{x}) u_j(\mathbf{x})\,\mathrm{d}\Gamma \tag{12}$$

where the collocation point $\boldsymbol{\xi}$ is on a smooth part of the boundary Γ, m_k are the components of the normal vector at $\boldsymbol{\xi}$, $D_{ikj}(\boldsymbol{\xi},\mathbf{x})$ and $S_{ikj}(\boldsymbol{\xi},\mathbf{x})$ are known functions of derivatives of $U_{ij}(\boldsymbol{\xi},\mathbf{x})$ and $T_{ij}(\boldsymbol{\xi},\mathbf{x})$, and the sign on the second integral indicates Hadamard principal value. Once more, depending on the type of analysis, different expressions are applicable to the tensors $D_{ikj}(\boldsymbol{\xi},\mathbf{x})$ and $S_{ikj}(\boldsymbol{\xi},\mathbf{x})$.

Again, in axisymmetric problems, the singularity behaviour of these tensors change depending on the position of $\boldsymbol{\xi}$ (de Lacerda and Wrobel, 2001). If the collocation point $\boldsymbol{\xi}$ is not at the axis of symmetry, the singular behaviour of these tensors can be expanded into the following expressions,

$$D_{ikj}(\boldsymbol{\xi},\mathbf{x}) = \frac{1}{\lambda} D^{2D}_{ikj}(\boldsymbol{\xi},\mathbf{x}) + D^{w}_{ikj}(\boldsymbol{\xi},\mathbf{x}) \tag{13}$$

$$S_{ikj}(\boldsymbol{\xi},\mathbf{x}) = \frac{1}{\lambda} S^{2D}_{ikj}(\boldsymbol{\xi},\mathbf{x}) + S^{s}_{ikj}(\boldsymbol{\xi},\mathbf{x}) + S^{w}_{ikj}(\boldsymbol{\xi},\mathbf{x}) \tag{14}$$

where the strongest singular terms are equivalent to two-dimensional ones, but less singular terms are also present. The term indicated by the superscript s is in fact a series of terms of strong singularity $O(|\mathbf{x}-\boldsymbol{\xi}|^{-1})$, while the others indicated by the superscript w contain weakly singular $O(\ln|\mathbf{x}-\boldsymbol{\xi}|)$ and regular terms. Using expressions (13) and (14) in the singular integrals of equation (12), the first integral can be split into a Cauchy principal value and a regular integral

$$\oint_{\Gamma} \lambda D_{ikj}(\boldsymbol{\xi},\mathbf{x}) t_j(\mathbf{x})\,\mathrm{d}\Gamma = \oint_{\Gamma} D^{2D}_{ikj}(\boldsymbol{\xi},\mathbf{x}) t_j(\mathbf{x})\,\mathrm{d}\Gamma + \int_{\Gamma} \lambda D^{w}_{ikj}(\boldsymbol{\xi},\mathbf{x}) t_j(\mathbf{x})\,\mathrm{d}\Gamma \tag{15}$$

while the second integral can be expanded into a Hadamard principal value, a Cauchy principal value and a regular integral

$$\neq\!\!\!\!\int_{\Gamma} \lambda S_{ikj}(\boldsymbol{\xi},\mathbf{x}) u_j(\mathbf{x})\,\mathrm{d}\Gamma = \neq\!\!\!\!\int_{\Gamma} S^{2D}_{ikj}(\boldsymbol{\xi},\mathbf{x}) u_j(\mathbf{x})\,\mathrm{d}\Gamma + \oint_{\Gamma} \lambda S^{s}_{ikj}(\boldsymbol{\xi},\mathbf{x}) u_j(\mathbf{x})\,\mathrm{d}\Gamma + \int_{\Gamma} \lambda S^{w}_{ikj}(\boldsymbol{\xi},\mathbf{x}) u_j(\mathbf{x})\,\mathrm{d}\Gamma \tag{16}$$

When $\boldsymbol{\xi}$ is on the z-axis, the radial component of the traction at this point must vanish and this can be directly obtained from the radial component of the traction boundary integral equation (12): $t_r(\boldsymbol{\xi}) = 0$. In the axial direction, the components $D_{zzj}(\boldsymbol{\xi},\mathbf{x})$ and $S_{zzj}(\boldsymbol{\xi},\mathbf{x})$ correspond to the three-dimensional ones. At $\boldsymbol{\xi}$, the radial component of the normal vector must be equal to zero and the traction equation (12) can be simplified to

$$\frac{1}{2}t_z(\boldsymbol{\xi}) = m_z \int_{\Gamma} \lambda D^{3D}_{zzj}(\boldsymbol{\xi},\mathbf{x}) t_j(\mathbf{x})\,\mathrm{d}\Gamma - m_z \neq\!\!\!\!\int_{\Gamma} \lambda S^{3D}_{zzj}(\boldsymbol{\xi},\mathbf{x}) u_j(\mathbf{x})\,\mathrm{d}\Gamma \tag{17}$$

where the first integral is, in fact, regular.

Since the primary objective of this work is to study the development of cracks from complex contact loadings, it is essential to have the contact and crack models coherently posed. Without loss of generality, the traction boundary integral equation is also written in incremental form

$$\frac{1}{2}\Delta t_i^k(\boldsymbol{\xi}) = m_l \oint_{\Gamma} \lambda D_{ilj}(\boldsymbol{\xi}, \mathbf{x}) \Delta t_j^k(\mathbf{x})\, \mathrm{d}\Gamma - m_l \neq\!\!\!\!\int_{\Gamma} \lambda S_{ilj}(\boldsymbol{\xi}, \mathbf{x}) \Delta u_j^k(\mathbf{x})\, \mathrm{d}\Gamma \tag{18}$$

Crack boundary conditions are usually traction free, and that may well be the case for the increments of growing cracks. Still, imposing these conditions is not straightforward in an incremental formulation, and details of these procedures are explained in the next section. In the simulations, microcracks are assumed to exist in the initial configuration and a full range of boundary conditions (Eqs. (5)–(8)) are applicable. The relevance of using these conditions, rather than simple traction free ones, is investigated in the analyses.

After the boundary discretization, Eqs. (4) and (18) are applied at crack nodal points, one on each side of the crack. At non-crack boundaries, only Eq. (4) is applied. A discretized system of equations is obtained where integrals over each element must be computed. Two types of integrations will appear: non-singular and singular. The first ones are computed using Gauss quadrature and the second requires different treatments, depending on which kernel of each equation is being integrated.

Generally speaking, the singularity subtraction technique (Davis and Rabinowitz, 1984) is used to regularize the integrand of all Cauchy and Hadamard principal value integrals. In this procedure, the integrals are transformed into regular or weakly singular, plus an improper integral suitable for evaluation by finite parts. Normal Gaussian integration is carried out for the regular integrals, while a local coordinate transformation (Telles, 1987) along with Gaussian quadrature is employed in the evaluation of the weakly singular ones. Evaluation of all improper integrals of two-dimensional functions is well documented in the literature, where direct (Portela et al., 1991; Guiggiani, 1995) or indirect (Lutz et al., 1990; Krishnasamy et al., 1990) methods may be applied. The present work uses the direct approach reported by Portela et al. (1991). The same approach is used to evaluate the extra CPV integral in axisymmetric analysis, where the exact singular behaviour of $S^s_{ijk}(\boldsymbol{\xi}, \mathbf{x})$ given by de Lacerda and Wrobel (2001) is fundamental.

An accurate evaluation of stress intensity factors is essential for crack trajectory simulations. These may be computed directly using special crack tip elements or in a post-processing level, as a function of the strain energy release rate G,

$$K_i = \sqrt{EG_i} \quad i = I, II \tag{19}$$

where E is the Young's modulus for plane stress and $E = E/(1-\nu^2)$ for plane strain and axisymmetric cases, with ν being the Poisson's ratio. Several methods have been proposed for the computation of G. In this work, the modified crack closure integral method (Rybicki and Kanninen, 1977) is adopted for its simplicity, speed and good level of accuracy. The method is based on an approximate evaluation of the crack closure integrals proposed by Irwin (1957):

$$\begin{aligned} G_{\mathrm{I}} &= \lim_{\delta a \to 0} \frac{1}{2\delta a} \int_{\delta a} \sigma_n \delta u_n \, \mathrm{d}a \\ G_{\mathrm{II}} &= \lim_{\delta a \to 0} \frac{1}{2\delta a} \int_{\delta a} \sigma_t \delta u_t \, \mathrm{d}a \end{aligned} \tag{20}$$

where δa is a small crack increment, σ_n and σ_t are the normal and tangential stresses along the path δa before the crack extension, and δu_n and δu_t are the relative normal and tangential displacements at the path δa after the crack extension. The approximation consists on taking displacements and stresses for a single crack configuration, rather than considering two crack lengths, a to obtain stresses and $a + \delta a$ to retrieve displacements. Assuming a as the crack tip element size or even a fraction of it, linear functions are used to interpolate gaps and relative tangential displacements along δa using the element nodal results. Opposite to the tip, in the same direction, stresses are calculated and interpolated in a similar manner over a virtual element of the same size δa. At first sight, linear functions may seem a poor representation, but they are in fact very adequate in a dual boundary element formulation, as reported by de Lacerda and Wrobel (2002).

4. Crack propagation model

Cracks will extend until stress intensity factors fall below the critical stress value K_T (toughness) of the material. Several criteria have been proposed to determine the direction in which cracks should propagate. Perhaps the most commonly used is the maximum principal stress criterion, which predicts that cracks will grow in a direction perpendicular to the maximum principal stress at their tip. With the knowledge of the stress intensity factor values K_I and K_{II}, this direction can be directly obtained from

$$\theta_c = 2\tan^{-1}\left[\frac{1}{4}\left(f \pm \sqrt{f^2+8}\right)\right] \quad f = K_I/K_{II} \tag{21}$$

where θ_c is measured from the crack axis ahead of the crack tip. Fracture instability occurs at a crack tip when the maximum principal stress reaches the toughness magnitude K_T. Assuming that an equivalent mode I stress intensity factor K_{Ieq} is responsible for the fracture process, the following expression is valid

$$K_{Ieq} = \cos^2\left(\frac{\theta_c}{2}\right)\left(K_I\cos\left(\frac{\theta_c}{2}\right) - 3K_{II}\sin\left(\frac{\theta_c}{2}\right)\right) > K_T \tag{22}$$

for this condition.

Once the directions are defined, crack increments are added to the system: a pair of elements for each extended crack. Their sizes are usually controlled as an increasing or decreasing function of the corresponding tip element size. Since the predicted angles θ_c do not take into account the length of the increments, corrections are necessary to adjust their orientations. This so-called predictor–corrector technique is an iterative procedure which requires an efficient method for the solution of the system, since this process will be repeated a great number of times. LU decomposition and the dual BEM can also be efficiently used in this crack propagation procedure (Portela et al., 1991). Prior to the incrementation, all current coefficients of the system have been decomposed and properly stored. When cracks are incremented, a few extra rows and columns are added to the system, and these new coefficients are the only ones to be decomposed. Actually, they are decomposed as many times as the increment elements are adjusted during the iterations, searching for the best θ_c values.

It was seen that an LU solver can be efficiently used in contact and crack analyses. In combined problems such as contact-induced crack propagation, the algorithm for the solution must be simultaneously efficient and a propagation algorithm is proposed in Fig. 1.

In this type of problem, before cracks start propagating, a certain amount of load has necessarily been applied. Consider this particular stage of the analysis, where k load steps have been applied and a certain number of iterations were performed to obtain the current contact status and overall solution. Let H_k denote the history of operations which transform the initial contact configuration into the current one (after k steps). As mentioned in the contact model section, this history of changes provides a series of modifications on the solution which can be quickly evaluated. Moreover, reapplying this group of operations is an even faster procedure since much of the computation during the first time has been stored.

The LU decomposition of the new coefficients in the propagation algorithm is stored alongside the original decomposed matrix. It is worth remembering that, originally, the system contained contact conditions for the initial configuration. After the system solution, results will correspond to the initial contact status, and a history of load increments and contact iterations must be applied to recover the current load stage P^k. Unfortunately, reapplying the operations H_k to the new slightly larger system is not sufficient to obtain the new results. These operations are likely to open the crack increments at load steps smaller than k, but somehow the increments must be kept closed until the fracturing moment when the load P^k is reached. This task differentiates the present combined contact-crack analysis from pure crack propagation, and overcoming this problem while maintaining efficiency is the key point of the present algorithm. The

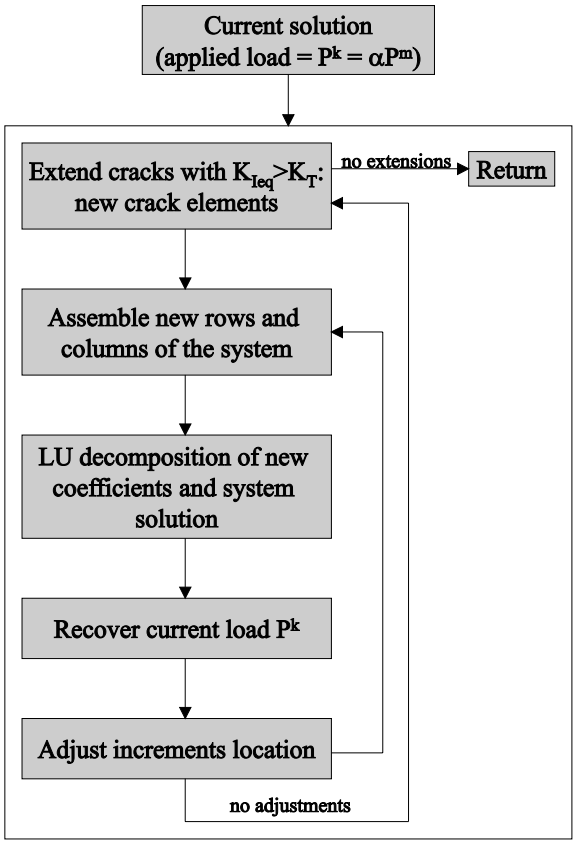

Fig. 1. Main structure of the algorithm of analysis.

approach used for this task is described in the next section, along with possible alternatives, and a discussion on advantages and disadvantages of each scheme.

Finally, the last step of the propagation algorithm corresponds to the angle adjustments of the crack increments. These corrections are necessary until a predefined tolerance is reached. This tolerance, which can be specified by the analyst, is the maximum allowed difference, in degrees, between the previous and the currently calculated direction of propagation (δ_θ). The smaller this value, the greater the number of angle iterations and computer time of the analysis. If any of the increments is tilted, the former new decomposed coefficients are discarded along with the last set of results, and the process is restarted from the assembly routine. The whole incremental process is repeated until $K_{\mathrm{Ieq}} < K_{\mathrm{T}}$ at all crack tips. When all cracks are arrested by the toughness of the relevant material, the analysis returns to the contact algorithm, possibly for further load increments and contact iterations.

5. Recovering the current load

At this point, cracks have grown and the number of unknowns in the system has increased proportionally to the number of extra elements. Basically, regarding the boundary conditions, elements can be of two types: simple boundary elements (fck, traction-free crack elements) with two unknown values per node,

or contact boundary elements (cck, contacting crack elements) with an additional two unknowns per node. The first type has one half of the number of unknowns compared to the second and this difference, in terms of computational speed, becomes relevant as the system is progressively expanded with the crack growth. Therefore, its use should be preferred; however, implementing it in the proposed incremental contact model is much more complicated. Tractions would have to be prescribed at these elements in order to keep increments closed up to the last step before their opening. These traction values are not known and would have to be calculated at a post-processing level, using results from the initial system. Furthermore, adapting these conditions to the external load-scaling process and elaborating a book-keeping format for the future crack increments to be added to the system, are enough reasons to discourage the use of this type of element in the present method. Nevertheless, a less accurate approach will later be discussed where these elements are used with some success. On the other hand, contact elements have been implemented with the load scaling and history of results in mind, and keeping the gaps closed at any stage is as simple as defining the elements to be in stick mode.

For simplicity, consider the single crack propagation case depicted in Fig. 2, although the following approach is general and easy to extend to multiple crack analysis. The top row of Fig. 2 shows a sketch of the crack growth process. The load is incremented $(a \rightarrow b)$ until the value P^k is reached, where the equivalent mode I stress intensity factor is greater than the toughness of the material. Next, the load is kept constant and the crack is extended $(b \rightarrow c)$ perpendicular to the maximum principal stress direction. In Fig. 2c, the mesh has two more contact elements, and new rows and columns are added to the system. After the decomposition of these new coefficients, the system is solved providing a solution vector $\mathbf{S}_0$, which represents the situation shown in Fig. 2d. The objective is to obtain the solution $\mathbf{S}_k$, which corresponds to

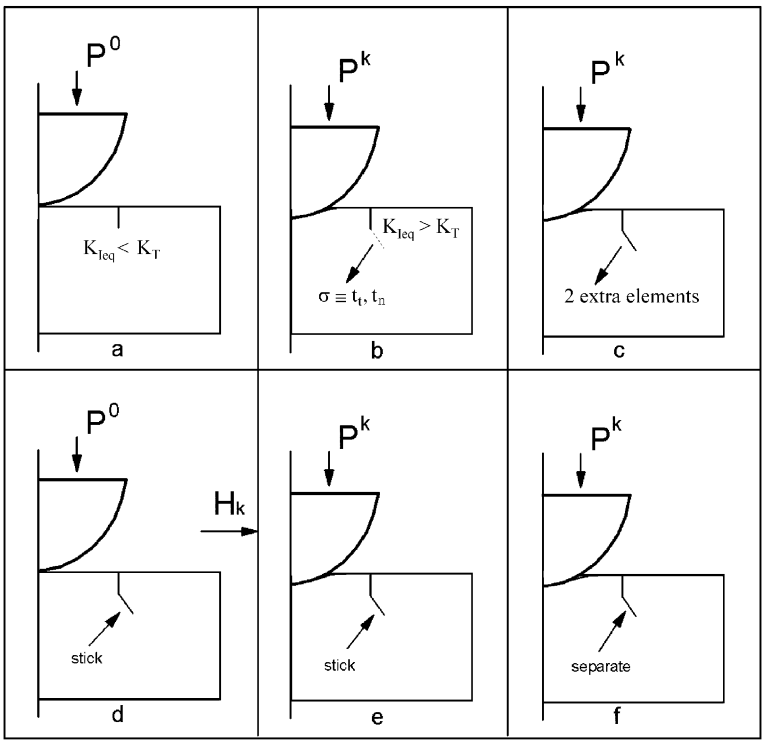

Fig. 2. Steps during crack propagation.

the load P^k with the new crack increment (Fig. 2f). In the new system, it is necessary that the new pair of elements behave as in stick mode until the crack opening stage, as depicted in the bottom row of Fig. 2. The computation of $\mathbf{S}_k$ is better visualized if performed in two steps: First, the solution $\mathbf{S}_0$ is transformed into an intermediate solution corresponding to Fig. 2e, through a series of known operations H^k. Second, the crack increment is simply released from stick mode $(e \rightarrow f)$ and contributions from this event are added to the intermediate solution, thus producing the final solution $\mathbf{S}_k$.

In practice, these two steps are independent from each other and can be simplified into a single faster step. The crack increment is set as a separate contact pair with zero gap in the first place, with compatibility conditions provided from post-processed stresses $t_j^{k,b}$ in the uncracked system in Fig. 2b,

$$\Delta t_j^k = -t_j^{k,b} \tag{23}$$

After decomposition and system solution, a different result for $\mathbf{S}_0$ is obtained and the simple application of H^k over this system, plus extra contact iterations if the status changes between configurations b and c, gives the solution $\mathbf{S}_k$. Apart from numerical errors, traction-free conditions $t_j^{k,f} = 0$ at the crack increment result within $\mathbf{S}_k$.

The load-scaling technique is based on calculating the load P^k which results in near zero normal tractions at the edge of the contact area. With the crack propagation, it is normal that changes on the contact stresses occur. The normal traction values at the edge will no longer be zero; however, the differences are normally negligible compared to the stresses in its vicinity.

5.1. Crack increments with simple boundary elements

Simple boundary elements (fck) can still be used for discretizating the increments by using a different approach. In this case, the previous history of increments and iterations H_k is completely discarded. A new incremental contact loading history is initiated and processed until the target load is reached. Recalculating the whole history can be very time consuming, specially because it has to be re-done after every correction. Still, this procedure is much faster than decomposing and solving the whole system with updated contact conditions. Compared to the formal approach with contact elements, the present one may even be faster if a large number of crack increments is added to the system. The main problem of this approach is the presence of the open crack increments at the beginning of the iterations, which does not occur in practice. For this reason, it is expected that the frictional contact stresses will be different from the real ones (frictionless analyses should not be affected). Another issue which may be influenced by this approach is the crack trajectories. These matters are investigated in the following examples.

It may be claimed that, if the previous approach cannot guarantee the correctness of the frictional stresses, then applying multiple load steps would not be essential. Instead, just a single load step could be used as an alternative, speeding up the analysis. This extra approximation certainly yields less accurate frictional contact stresses, compared to the multiple steps case.

6. Contact-induced crack propagation analyses

A number of indentation tests were numerically simulated to verify the accuracy and efficiency of the proposed formulation. Results are compared with simple theoretical formulae, when available, and with numerical results from previous simulations by other authors.

Three types of axisymmetric indenters are used in the numerical tests: a sphere (sph), a machined sphere (ms) and a cylinder (cyl). The first indenter has a radius of 1.98 mm and produces a non-conforming type of contact, with an increasing contact area as the load is augmented. The second indenter has the same radius

Table 1
Monoliths material properties

Material	Soda-lime glass	Silicon nitride	Fused silica
Young's modulus (MPa)	69,000	335,000	70,000
Poisson's ratio	0.21	0.27	0.14
Fracture toughness (MPa $m^{1/2}$)	0.75	3.9	1.9

and a flat base of 1 mm radius. The last indenter has a height also equal to 1.98 mm, and the same contacting area as the second. The same material was employed for the three indenters—Tungsten carbide with Young's modulus of 614 GPa and Poisson's ratio equal to 0.22. The cracked specimen is an axisymmetric monolith, with radius and height equal to 20 mm. These dimensions were verified to be sufficiently large to avoid boundary influences over the propagating cracks. Three types of brittle materials were tested and their properties, including their fracture toughness, are presented in Table 1. In the contact area, non-dimensional friction values of 0.05, 0.1, 0.2 and 0.3 were employed, besides some frictionless analyses.

In the first validation test, the machined spherical indenter is pressed against the three types of monolith and a further, hypothetical one, with Poisson's ratio equal to 0.4 and an arbitrary Young's modulus. The contact is assumed to be frictionless, and a tiny crack $c = 10$ μm long is imposed normal to the top surface of the monolith, distant from the axis of symmetry by $r_0 = 1.1$ mm. A total of 213 linear elements were used for the model discretization, with 10 along the initial crack (5 on each side) and 40 along each contacting surface. A 10 kN load was applied in a single step, and a total of 80 crack increments were allowed to propagate. As expected, cone cracks were formed as shown in Fig. 3. Note the different angles they make with the horizontal direction, which increase in an inverse proportion to the Poisson's ratio. The angle obtained in the case of the soda-lime glass monolith is approximately the same reported by Kocer and Collins (1997), while all the others match the values reported by Bush (1999).

The second set of tests include a comparison between the two flat base indenters, for different friction values. The boundary element mesh was identical to the previous case, and the monolith material used was soda-lime glass. In the crack trajectories in Fig. 4, the angle of propagation was the same as before for the

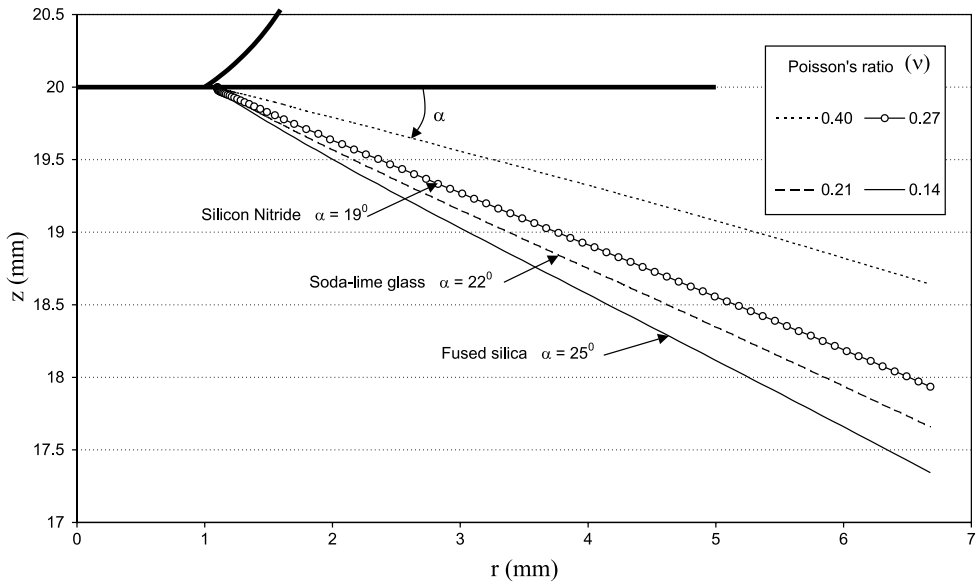

Fig. 3. Cone angles formed during indentation of different materials.

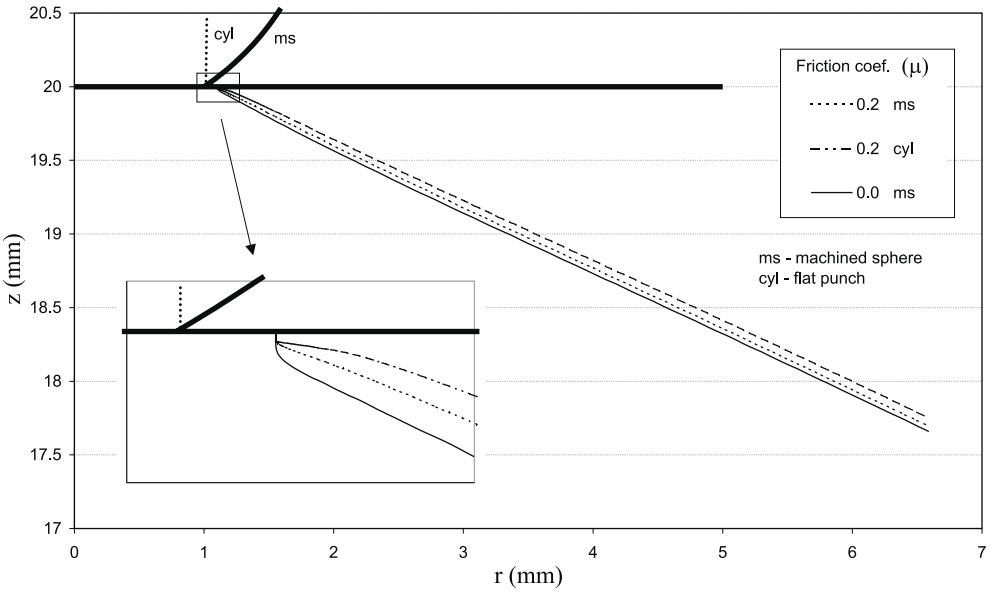

Fig. 4. Effect of friction and indenter type on crack propagation.

different combinations. However, it is interesting to notice that the trajectories are slightly offset from each other. This effect can be attributed to the influence of friction and the indenter geometry at the onset of the propagation. In the machined indenter case, the crack tends to find the cone angle before the cylindrical indenter case, i.e. with a smaller amount of applied load. The effect of friction is to keep the initial crack faces in contact, with a larger mode II stress intensity factor required for the initial development of the crack, as expected.

The two flat indenters are also used to simulate the correlation between the applied load (P) and the base radius (R) of the cone crack, for the soda-lime monolith. The following expression is valid when R is sufficiently larger than the indenter radius (Lawn, 1993),

$$P^2 = \alpha R^3 \tag{24}$$

where α is a constant depending on the Poisson's ratio and fracture toughness of the cracked specimen. In Fig. 5, results for both indenters with frictionless contact conditions, and the cylindrical indenter with friction $\mu = 0.05$, compare well with the asymptotic expression (24) in the specified range. Notice that the cylindrical indenter without friction appears to be in closer agreement, but although the other two results seem to be slightly outside, their slope is very similar to the expected one. This behaviour matches the observations in Fig. 4, where the cones are slightly offset. At the beginning of propagation, a 'pop in' effect can be observed. This phenomenon is well reported in the literature and corresponds, in Fig. 5, to the gaps between data at small values of R. Another point in agreement with observations in Fig. 4 is that a higher load was needed to initiate the propagation for the machined sphere, and an even higher one for the cylinder with friction, compared to the cylinder without friction. In fact, a much higher load was needed for the cylinder with friction, resulting in a larger 'pop-in' effect.

This behaviour is clarified in Fig. 6 which shows a plot of the normalized strain energy release rate as a function of crack length, following Mauginot and Maugis (1985) and Lawn (1993), for different values of the contact friction parameter. Two sets of curves are presented, for $r_0/a = 1.1$ and 1.3, where a is the

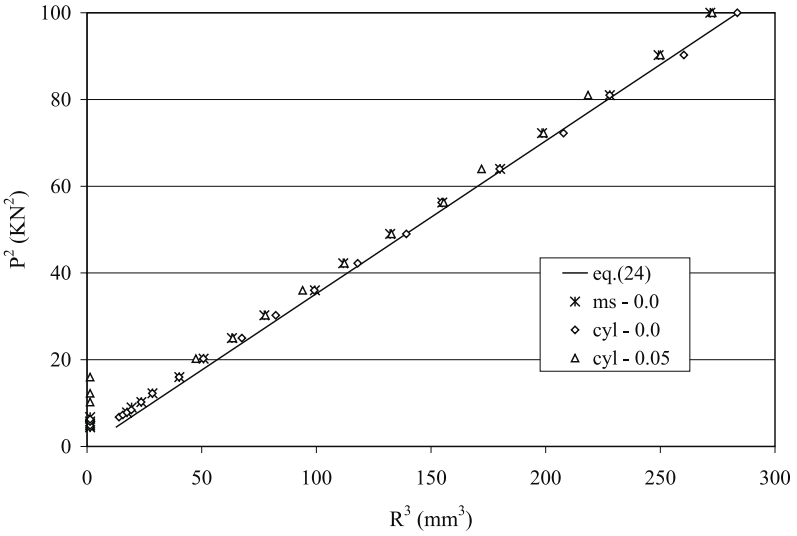

Fig. 5. Relation between applied load and cone crack base radius for the conforming type of contact.

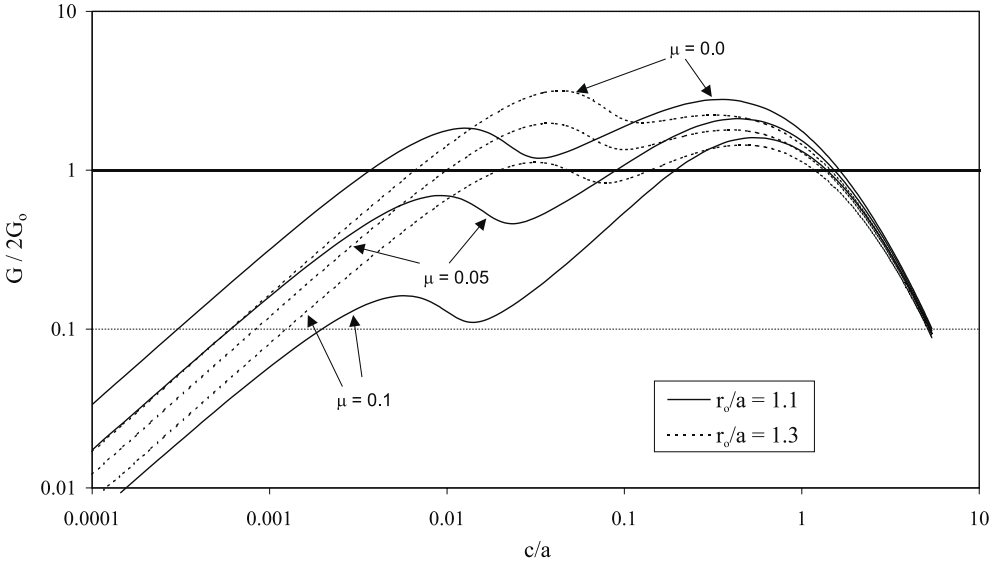

Fig. 6. Cylindrical punch. Normalized strain energy release rate against c/a for two starting locations of the crack and different contact friction values.

cylinder radius. Although plots were only produced for a single load case, higher or lower indentation loads would simply shift the curves upwards or downwards, respectively (Mauginot and Maugis, 1985). The first crossing points between the curves and the stability line $G/2G_0 = 1$ (G_0 is the fracture surface energy) indicate the normalized crack length necessary to initiate propagation. It is clear that, in both cases, this length must be greater as friction increases. Alternatively, for a fixed crack length, increasing friction means that a higher load would be required to initiate propagation. It can be observed in Fig. 6 that all curves

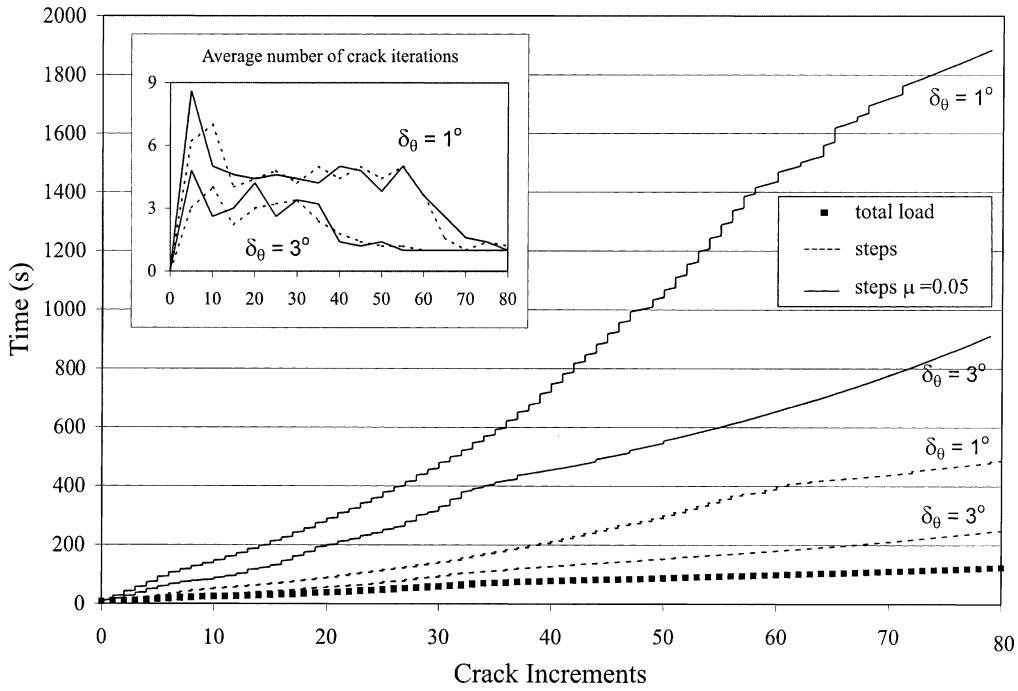

Fig. 7. Influence of friction, crack angle tolerance iteration and number of load steps on the performance of the algorithm.

present two peaks, a characteristic feature of cylindrical punches, and that the amplitude of the first peak increases with the ratio r_0/a, in agreement with the results of Mauginot and Maugis (1985).

Fig. 7 presents the accumulated CPU time (on a Pentium III-750/128Mb) for the propagation of 80 crack increments in the soda-lime monolith, induced by the cylindrical indenter, under different circumstances. It is clear that applying all the load in one single step (total load) is faster than using several steps. Therefore, in a conforming type of contact, this approach should be preferred if only the crack trajectory is sought. If a correlation between load and crack size is required, then load steps are necessary. In this case, it can be seen that the numerical procedures are much more time consuming when friction is considered. The main reasons are the greater number of contact iterations to define the stick–slip partition, and the longer time needed to compute the operations H^k to obtain the solution at the kth load step. Another factor that can be observed is the influence the crack increment angle error tolerance (δ_θ) has on the CPU time. An analysis with an error tolerance of 3° is approximately twice faster than using 1°. This factor can be verified in the insert to Fig. 7, where a larger number of crack (angle) iterations are needed for the 1° case. This figure also shows that, after a certain number of increments, the number of crack iterations reduces to nearly one. This happens when the crack finds its straight direction of propagation.

Results for the non-conforming indentation test of a silicon nitride monolith block are depicted in Fig. 8, alongside theoretical and experimental trend lines. In this test, the initial crack is 8 μm long and 0.351 mm distant from the axis of symmetry. The dual BEM results for the indenter load (P) versus the crack length (C) seem to converge to the theoretical far-field relation. However, as previously observed by Bush (1999), the numerical results deviate from the experimental ones (Lee et al., 1997) as a result of plastic deformation within the indenter. Two regions of unstable crack growth at the onset of propagation were detected in this test. The applied load was never reduced during indentation, and this explains the gaps between data indicated by these regions. The first gap is between the initial crack location (dashed line) and the initial

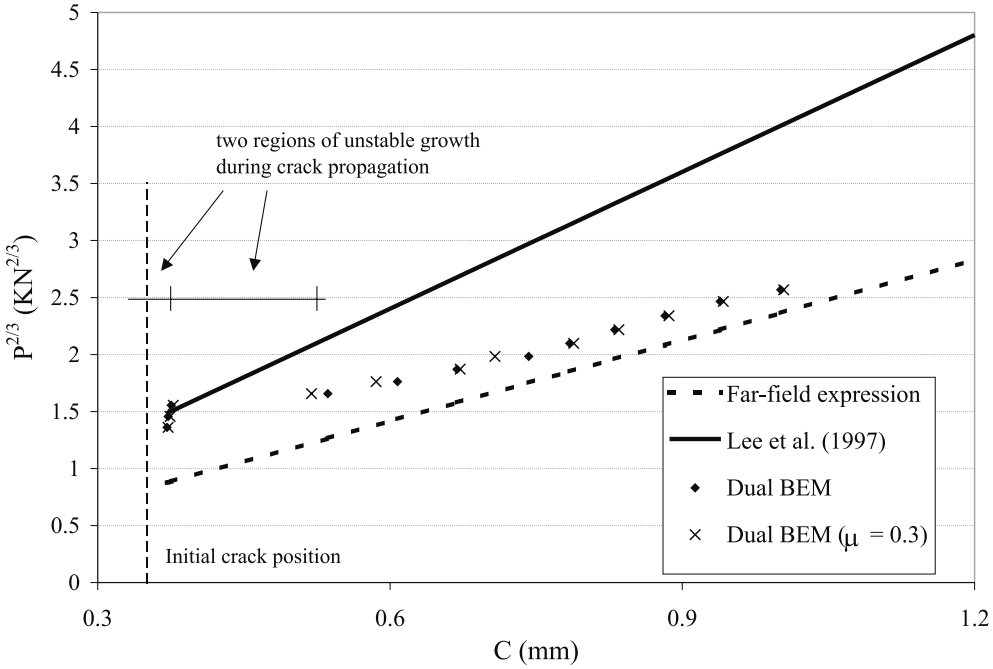

Fig. 8. Relation between applied load and cone crack length on the spherical indentation.

marks of the two presented results. The second gap is between the initial data marks and the fourth mark of each result. The two regions together correspond to the 'pop-in' effect commonly observed in experimental tests. It can be seen that the introduction of friction in this test was not significant at all. Neither the crack trajectories nor the minimal load for the 'pop-in' were substantially different. The minimum load necessary to initiate crack propagation was found to be $P = 1.59$ kN, which is quite close to experimental observations (Lee et al., 1997), even though the initial crack size (8 μm) may not be the most appropriate and the formulation is not particularly well suited for this analysis, due to the absence of plasticity.

The accumulated CPU times for the propagation of 36 crack increments in the previous non-conforming test are shown in Fig. 9. An angle error tolerance $\delta_\theta = 1°$ was adopted, and two types of crack elements were used to model the system: contacting crack elements (cck) and contact-free crack elements (fck). As expected, the use of fck elements for crack growth speeds up the analysis, since they involve a smaller number of unknowns. The load-scaling technique is used in this test, and it can also be seen that the introduction of friction delays the analysis, whatever type of crack elements are employed. The crack trajectories for the cases analysed are shown in the insert to Fig. 9. Neither the friction in the contact area, nor the type of crack element, seem to affect the crack path. Three zones are indicated in this figure. In the first, the curves are nearly horizontal, meaning that only a small number of contact and crack direction iterations are necessary. This effect continues until the crack growth reaches the compression area formed in the monolith. The second zone corresponds to the deviation of the propagating crack to avoid the compressive area. In this process, a larger number of crack direction iterations is needed, resulting in a steeper curve. In the third zone, the crack reaches its straight path, and the curve slope increases as more crack increments are added to the system.

The frictionless cases needed not be incremental, and a single load step should be sufficient for the analysis. As for the added crack elements, the fck type of elements is also appropriate. On the other hand, for frictional problems, the applied indenter load has to be incremental, and fck elements cannot produce a

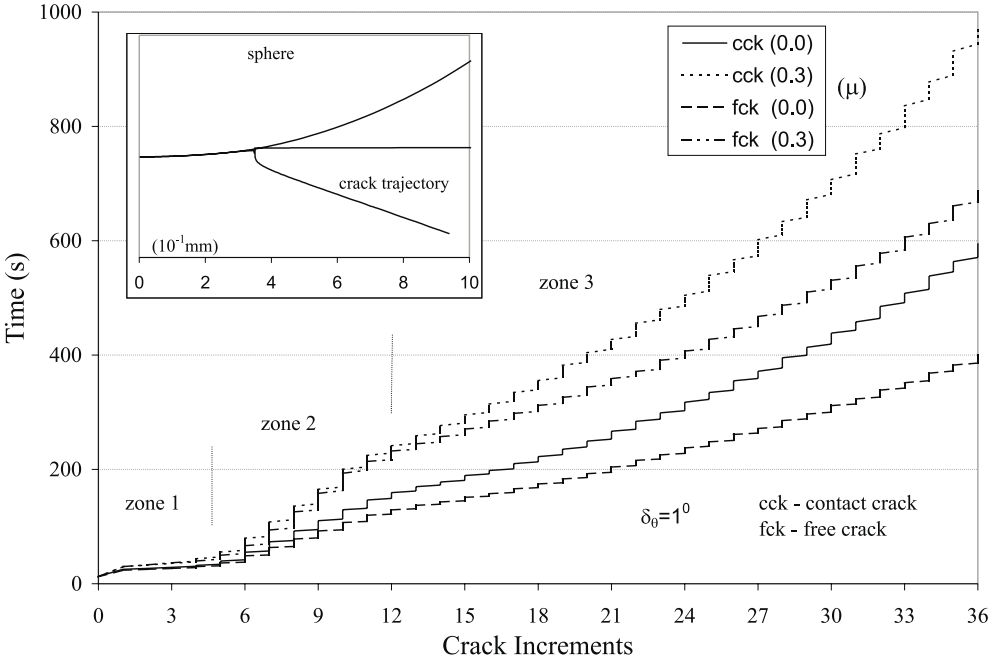

Fig. 9. Influence of friction and choice of crack element increment on the performance of the algorithm.

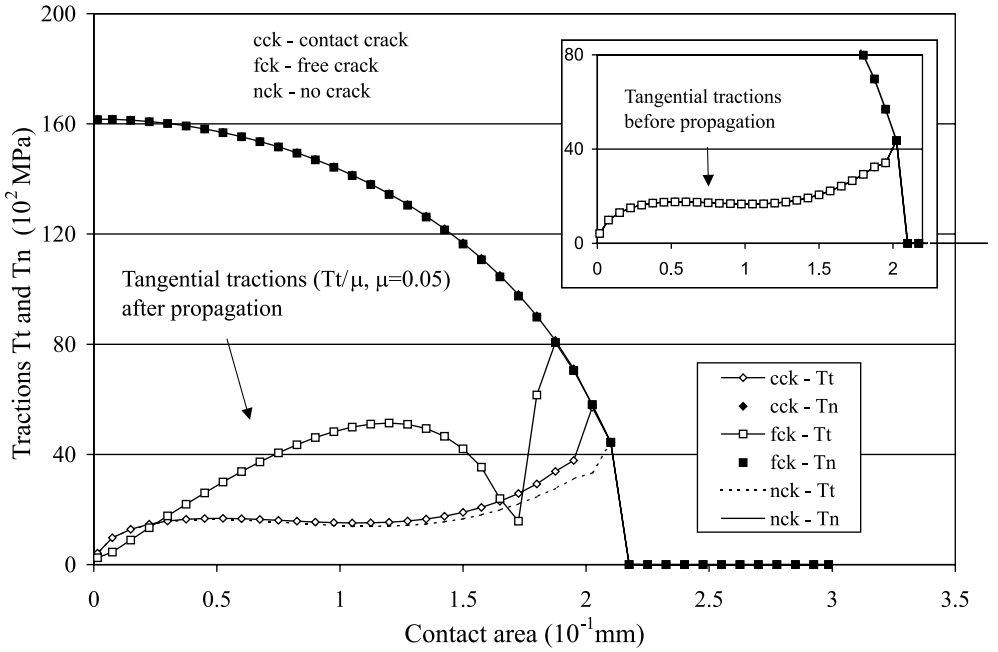

Fig. 10. Influence of the choice of crack element increment on the tangential tractions development.

completely correct result as can be seen in Fig. 10. A friction value of $\mu = 0.05$ was used in the same non-conforming test, and no differences were noticed for the normal contact tractions. Prior to the crack

propagation, tangential tractions were the same whether fck or cck elements were used. After the initial crack propagation, the analysis with cck elements closely matches the same contact problem without the crack (nck). However, when fck elements are used, the tangential traction values are very different from the previous results. This behaviour was expected as reported in the previous section, despite the lack of plasticity in the analysis.

7. Conclusions

Boundary element algorithms for the analysis of contact-induced crack propagation problems have been developed. For this purpose, axisymmetric formulations for contact and crack analyses were coupled in an incremental manner. Conforming and non-conforming frictional contact are considered, and the dual boundary element method is used in the crack modelling, allowing the analysis of crack propagation in a faster and elegant manner.

An efficient approach is employed to retrieve the solution with speed and accuracy. Once the initial system is solved, contact iterations are quickly performed to obtain the extension of the contact area and the stick–slip partition. For the crack formulation, the original system is maintained and enlarged as more crack elements are added to the problem. The initial system decomposition and the contact history of iterations are also accounted for in the solution, after every crack increment.

The influence of the choice of crack elements in the solution speed and accuracy was demonstrated in the numerical tests. It was observed that crack elements with contact capabilities are essential in some cases. The influence of the geometry of the indenter and the friction in the contact area was also analysed.

In general, results from the indentation tests studied here compared well with available experimental, theoretical and numerical data. The lack of plasticity in the present formulation seems to be the main reason for the mismatch in the load versus crack length results for the non-conforming indentation case. Future investigations will address this particular problem and the influence of plastic deformation due to high stress concentrations at the edges of flat punches. Finally, the algorithms proved to be quite efficient, and capable of accurately simulating indentation tests.

References

Abdul-Mihsein, M.J., Bakr, A.A., Parker, A.P., 1986. A boundary integral equation method for axisymmetric elastic contact problems. Computers and Structures 23, 787–793.

Andersson, T., 1981. The boundary element method applied to two-dimensional contact problems with friction. In: Proceedings of the Third International Seminar on Boundary Element Methods. Springer, Berlin.

Bush, M.B., 1999. Simulation of contact-induced fracture. Engineering Analysis with Boundary Elements 23, 59–66.

Davis, P.J., Rabinowitz, P., 1984. Methods of Numerical Integration. Academic Press, New York.

de Lacerda, L.A., Wrobel, L.C., 2000. Frictional contact analysis of coated axisymmetric bodies using the boundary element method. Journal of Strain Analysis for Engineering Design 35, 423–440.

de Lacerda, L.A., Wrobel, L.C., 2001. Hypersingular boundary integral equation for axisymmetric elasticity. International Journal for Numerical Methods in Engineering 52, 1337–1354.

de Lacerda, L.A., Wrobel, L.C., 2002. Dual boundary element method for axisymmetric crack analysis. International Journal of Fracture 113, 267–284.

Ezawa, Y., Okamoto, N., 1989. High-speed boundary element contact stress analysis using a supercomputer. In: Proceedings of BETECH'89. Computational Mechanics Publication, Southampton.

Guiggiani, M., 1995. Hypersingular boundary integral equations have an additional free term. Computational Mechanics 16, 245–248.

Irwin, G.R., 1957. Analysis of stresses and strains near the end of a crack traversing a plate. Journal of Applied Mechanics 24, 361–364.

Kocer, C., Collins, R.E., 1997. The angle of Hertzian cone cracks. Journal of the American Ceramic Society 81, 1736–1742.

Krishnasamy, G., Schmerr, L.W., Rudolphi, T.J., Rizzo, F.J., 1990. Hypersingular boundary integral equations: some applications in acoustic and elastic wave scattering. ASME Journal of Applied Mechanics 57, 404–414.

Lawn, B.R., 1993. Fracture of Brittle Solids, second ed. Cambridge University Press, Cambridge.

Lee, S.K., Wuttiphan, S., Lawn, B.R., 1997. Role of microstructure in Hertzian contact damage in silicon nitride: (i) Mechanical characterization. Journal of the American Ceramic Society 80, 2367–2381.

Lutz, E.D., Gray, L.J., Ingraffea, A.R., 1990. Indirect evaluation of surface stress in the boundary element method. In: Proceedings of IABEM'90. Springer, Berlin.

Mauginot, R., Maugis, D., 1985. Fracture indentation beneath flat and spherical punches. Journal of Materials Science 20, 4354–4376.

Portela, A., Aliabadi, M.H., Rooke, D.P., 1991. The dual boundary element method: effective implementation for crack problems. International Journal for Numerical Methods in Engineering 33, 1269–1287.

Rybicki, E.F., Kanninen, M.F., 1977. A finite element calculation of stress intensity factors by a modified crack closure integral. Engineering Fracture Mechanics 9, 931–938.

Telles, J.C.F., 1987. A self-adaptive co-ordinate transformation for efficient numerical evaluation of general boundary element integrals. International Journal for Numerical Methods in Engineering 24, 959–973.

Wrobel, L.C., Aliabadi, M.H., 2002. The Boundary Element Method. Wiley, Chichester.